Large and Small Scale Structure in Rayleigh-Taylor Mixing

Marilyn B. Schneider, Guy Dimonte, and Bruce Remington

Lawrence Livermore National Laboratory, Livermore, California 94551

(Received 24 April 1997; revised manuscript received 4 December 1997)

Laser-induced fluorescence is used to image the central plane of the mix region of two immiscible liquids subject to the Rayleigh-Taylor instability at an acceleration of 70 times Earth's gravity. The size of the mixing zone grows with coefficient $\alpha_b \gtrsim 0.054$. Individual bubbles are clearly resolved and their structure is measured. The widths of the bubbles are narrower than recent models predict. An internal structure in the bubbles appears after the mixing zone is established. This structure suggests a cascade to small wavelengths. The cascade is required for molecular mix. [S0031-9007(98)05869-4]

PACS numbers: 47.20.Ma, 47.20.Ky

If two fluids are accelerated at a rate g such that the lighter fluid of density ρ_1 pushes the heavier fluid of density ρ_2, any irregularity at the interface will grow. This is the Rayleigh-Taylor (RT) instability [1,2]. It determines the shape of type-II supernova explosions [3]; it leads to premature mixing of inertial confinement fusion (ICF) targets [4]; it also appears in terrestrial and nuclear physics, as summarized in Ref. [5].

In the RT instability, small amplitude perturbations at the fluid interface grow as $\sim\exp(\sqrt{Akg}\,t)$ where k is the wave number, A is the Atwood number $(\rho_2 - \rho_1)/(\rho_2 + \rho_1)$, and t is the time since g began [2,6]. At amplitudes larger than $\sim 1/k$, the modes grow more slowly and couple nonlinearly [5,7–9]. A highly disordered mixing zone (DMZ) eventually develops in which the initial conditions are forgotten. The size of the DMZ and the large scale structures within it then scale with the single characteristic length Agt^2. It is also presumed that shear and inertia produce a cascade to smaller wavelengths [9–11]. This cascade is important because it leads to molecular mix which determines the constitutive properties in the DMZ such as composition (or density), energy, effective opacity, and equation of state. The time at which this cascade occurs is unknown.

The extent of the DMZ is defined by a bubble front which penetrates the heavy fluid as $h_b \sim \alpha_b Agt^2$ and a spike front which penetrates the light fluid as $h_s \sim \alpha_s Agt^2$ [10,12–16]. The coefficient α_b is insensitive to A whereas α_s increases with A [10,15]. Experiments [12–14,16] using backlit photography obtain values of $\alpha_b \sim 0.06$–0.07 that are larger than those found in 3D [10,17] and some 2D [12,17,18] hydrodynamic simulations, and a two-phase flow model [19] but similar to those found in 2D simulations which track the interface [20,21].

The average width of the large scale bubbles in the DMZ is observed in backlit photographs to grow with mix width [13,16], but measurements of individual bubbles have not been made. Backlit photography cannot measure configurations within the DMZ so the cascade has not been directly seen experimentally [10].

This Letter describes RT experiments using laser-induced fluorescence (LIF) which image the DMZ between two immiscible liquids at Reynolds number of order $\sim 10^5$. This Letter shows (i) the measured α_b is consistent with recent experiments [16], (ii) the measured large scale bubble and spike widths increase with the size of the DMZ but are narrower than models predict, and (iii) there is an internal structure in the bubbles and spikes which appears after the DMZ is established and whose average size remains constant late in time.

The experiments use the Linear Electric Motor (LEM) [22] at Lawrence Livermore National Laboratory to accelerate a container for 50 ms at a downward constant $g \sim 73 g_0$ (g_0 = Earth's gravity). The fluid cavity is 73 mm wide, 88 mm high, and 73 mm deep. For LIF, a laser sheet parallel to the acceleration illuminates the central plane of the cavity from below. Images of the fluorescence are recorded on 35-mm film.

The film images are digitized, converted to intensity images, corrected for the absorption of the laser light by dye molecules in the fluid, smoothed to reduce noise, and adjusted for variations in the laser intensity across the cell. To avoid wall effects, only the central 62-mm width of the cell is analyzed.

The fluids are decane ($\rho_1 = 0.73$ g/cm^3), and salt water ($\rho_2 = 1.43$ g/cm^3) plus a small amount of fluorescent dye (Kiton Red 620), giving an Atwood number of $A = 0.34$. The surfactant AOT is added to lower the interfacial tension to ultralow values by forming a microscopically thin microemulsion phase [23] at the interface. Glucose is added to the salt water to match its refractive index to within 0.03% of that of decane.

Corrected film density images at 27 and 45 ms are shown in the first column of Fig. 1. The net displacement of the cell due to the acceleration is Z so the characteristic length is $Agt^2 = 2AZ$. The planar coordinate system moving with the cell is x, z, with $z = 0$ at the original interface.

The interfacial tension σ stabilizes the RT growth of perturbations with small wavelengths, leading to a mode of fastest growth with wavelength $\lambda_{\mathrm{FG}} = 2\pi\sqrt{3/2}\,\ell_c$, where ℓ_c is the capillary length $\ell_c^2 = 2\sigma/[(\rho_2 - \rho_1)g]$ [24]. In the present experiment, $\ell_c = 0.10$ mm at $73 g_0$, so $\lambda_{\mathrm{FG}} \sim 0.7$ mm with an e-folding time [24] ~ 0.9 ms.

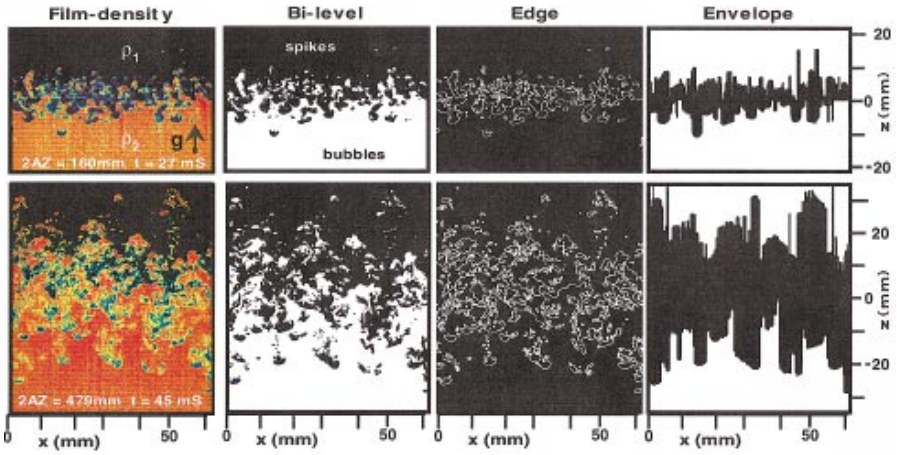

FIG. 1(color). Images from a single run at two times illustrating the various types of processed images. The corrected film-density images are used to generate the bilevel images. The bilevel images are used to generate the edge images and the envelope images.

When the amplitude becomes $\sim 1/k \sim 0.1$ mm, the mode saturates. Thus, by 27 ms (the top image in Fig. 1), the system has evolved into the DMZ regime.

The images are processed (Fig. 1) into bilevel and edge images to emphasize the internal structures, and envelope images to display the large scale features. The bilevel image is generated from the corrected film-density image by mapping all pixels with less than $\sim 50\%$ intensity to 0%, and all pixels with greater than $\sim 50\%$ intensity to 100%. The cutoff level used for the mapping is chosen to keep the same number of pixels in each fluid (conservation of volume). The bilevel image is used to generate (i) the edge image using the Roberts edge method [25] and (ii) the envelope image using single-valued (in x) bubble and spike envelopes. The lower (bubble) envelope function is obtained by finding the value of z at which the maximum penetration of the top fluid into the bottom fluid occurs. The spike envelope is similar but on top. In the envelope image, the region between the two envelope functions is shown in black to mimic the backlit photographs [12–14,16]. The resolution of the processed images is <1 mm [26].

The width of the DMZ is obtained from the bilevel image. Backlit photographs [12–14,16] obtain the width by measuring the penetration of the bubble and spike fronts. The present data sample only one plane of the DMZ, so fewer bubbles and spikes are observed. To overcome the reduced statistics, a new penetration depth is defined from the projection of the bilevel image onto the z axis, as shown in Fig. 2. The projection is plotted as a density profile and generally has many fluctuations, so it is fit to a straight line. The bubble (spike) penetration h_b (h_s) is defined as the distance between the intersection of the straight line with ρ_2 (ρ_1) and the original location of the flat interface ($z = 0$). The latter can be measured to within ~ 1 mm. The present definitions of h_b and h_s are statistically robust because they depend on the entire profile.

The variation of h_b and h_s with $2AZ$ appears linear, as shown in Fig. 3. This collection of data represents six separate runs, recording three images per run. The errors are the same size as the plot symbols and are due to the uncertainty in the location of the original interface. The data are fit to straight lines [13,18], $h = h_0 + \alpha 2AZ$. The linear fits in Fig. 3 give $\alpha_b = 0.054 \pm 0.003$ and $\alpha_s = 0.062 \pm 0.003$. The value of α_b is $\sim 10\%$ smaller than the $\alpha_b = 0.061$ obtained in backlit photography [16], which is shown as the upper dashed line in Fig. 3(a). This is expected because the laser sheet may not illuminate the most penetrating bubbles or spikes or their tips. This effect is greater later in time when there are only a small number of bubbles (2–4) with large penetrations. Thus, backlit photography is not seriously contaminated by wall effects. The present measurement of α_b is $\sim 7\%$ higher than the $\alpha_b = 0.05$ obtained found in 3D hydrodynamic simulations [10,17], as shown in the lower dashed line in Fig. 3(a). The simulations obtain h_b and h_s from the 99%, 1% [10] points of a volume-fraction profile. The simulation results appear to be low.

Finally, the ratio $h_s/h_b \approx 1.1 \pm 0.05$ is obtained by calculating h_s/h_b for each data point. The error bars

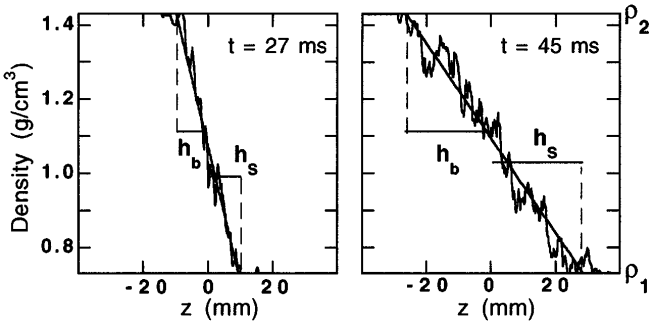

FIG. 2. The projection of the bilevel images of Fig. 1 onto the z axis. The projection is normalized to the density of the fluids. The definitions of bubble (h_b) and spike (h_s) penetration distances are shown.

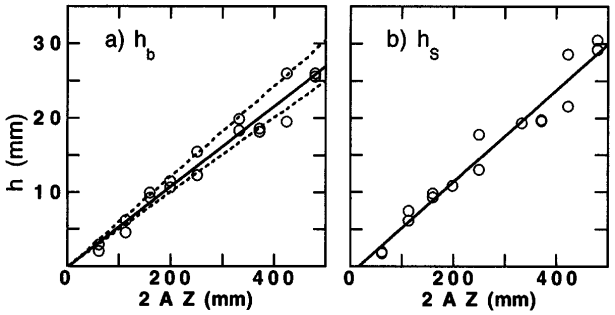

FIG. 3. (a) Bubble h_b and (b) spike h_s penetrations vs the characteristic length $2AZ$. The solid lines are (a) $h_b = -0.45 + 0.054(2AZ)$ and (b) $h_s = -0.95 + 0.062(2AZ)$. The dashed lines in (a) show $\alpha_b = 0.061$ (upper line) and 0.05 (lower line).

reflect the sensitivity of this ratio to the location of the flat interface. This ratio is in agreement with previous data [12] and 3D simulations [10] but lower than the 1.3 predicted from 2D simulations [21] and models [15,27] for $A = 0.34$.

The images in Fig. 1 suggest that the widths of the bubbles and spikes increase with time. This is clearly seen in the envelope images, which are used to measure the bubble widths. The + symbols in Fig. 4(a) show the widths of bubbles with penetrations greater than $\sim 0.82h_b$ versus $h_b + h_s$. There is much scatter in data, but the bubble widths *do* increase with $h_b + h_s$.

The size of structures can also be deduced from the bilevel image by calculating its correlation function $\mathcal{A}_x$ in the x direction. Let $A_x(x', z_1)$ be the correlation function of a horizontal line at $z = z_1$. Then $\mathcal{A}_x$ is the sum over all A_x's:

$$\mathcal{A}_x(x') = \sum_{z1} A_x(x', z_1) = \sum_{z1} \sum_{x} \mathrm{IMG}(x, z_1)\mathrm{IMG}(x + x', z_1),$$

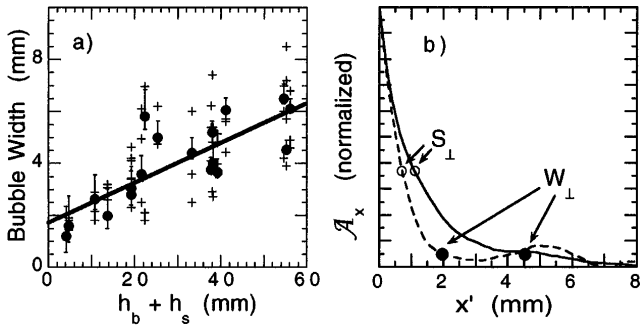

FIG. 4. The large scale structure size. (a) The individual bubble widths (+), measured from the envelope images vs $h_b + h_s$. (b) The correlation function $\mathcal{A}_x$ vs x' obtained from (– – – –) early and (———) late time bilevel images in Fig. 1. $S_\perp$, the e^{-1} width, and $W_\perp$, the 5% width, are indicated. The filled symbols in (a) are the measured $W_\perp s$. The straight line in (a) is $\langle W \rangle = 1.7$ mm $+ 0.077(h_b + h_s)$.

where $\mathrm{IMG}(x, z)$ is the pixel value, either black or white, at (x, z). The actual calculations minimize aliasing and correct for the finite sample size as described in Ref. [26].

Figure 4(b) shows the normalized $\mathcal{A}_x$ vs x' for the two bilevel images in Fig. 1. The shape of $\mathcal{A}_x$ is determined by the underlying size distribution of structure widths. The present study chooses to characterize $\mathcal{A}_x$ by its e^{-1} width, $S_\perp$, and its 5% width, $W_\perp$. Calculations [26] on bilevel images of sample distributions show that the average width of structures is $\sim 2-3S_\perp$ and that $W_\perp \sim 2-3S_\perp$ if the underlying size distribution has a single characteristic length. For an underlying size distribution with some long-length tail, $2-3S_\perp$ is the average size of structures and $W_\perp \sim$ the size of the largest structures. For the present data, $W_\perp \sim 3S_\perp$ until $h_b + h_s \sim 30$ mm and then $W_\perp/S_\perp$ increases with $h_b + h_s$. Late in time, therefore, $S_\perp$ and $W_\perp$ are measuring two different sizes. $2S_\perp$ is approximately the average width of the internal structures, whereas $W_\perp$ is the average width of the larger structures, the bubbles and spikes. (The bubbles and spikes are treated the same in these calculations because $h_b \approx h_s$.)

Figure 4(a) shows this interpretation of $W_\perp$ is valid because $W_\perp$ (filled circles) agrees with the measured individual bubble widths. The straight line fit to $W_\perp$ is ≈ 1.7 mm $+ 0.077(h_b + h_s) \approx 1.7$ mm $+ 0.15h_b$ (using $h_b \approx h_s$), but there is scatter of $\pm 50\%$.

The ratio of bubble penetration to bubble size is a parameter of many models [9,15,20,28–30], but the definition used varies widely. In this Letter, the measured ratio is $h_b/W_\perp \approx 2-6$ consistent with Mikaelian's analytical model [11]. The Glimm-Sharp bubble merger model [9,20,29] uses R_c, the radius of curvature of the bubble tip as a measure of bubble size, and predicts $h_b/2R_c \approx 1$ [30]. In the bubble-interaction model of Alon *et al.* [15] $h_b/\langle \Lambda \rangle = 0.5/(1 + A) \approx 0.4$, where $\langle \Lambda \rangle = P_0/n$ (P_0 = width of the image and n = number of rising bubbles in the image). This predicts an average of 2–3 rising bubbles in the images in the top row of Fig. 1, and ~ 1 rising bubble in the images in the bottom row. This appears inconsistent with our observations.

The internal structure, seen in the bilevel and edge images of Fig. 1, has an average width of $\sim 2S_\perp$. Figure 5(a) shows that $2S_\perp$ levels off when $h_b + h_s \sim 30$ mm or $2AZ \sim 270$ mm. A different aspect of the internal structure is measured by the amount of contact area between the mixing fluids. The contact area is important because it determines the opportunities for particle and energy exchanges. In the 2D edge image in Fig. 1, the contact area reduces to the perimeter P, that is, the length of the white pixels. Figure 5(b) plots $P - P_0$ vs $h_b + h_s$. (P has been reduced by 20% to correct for digitization errors.) The data are fit to a straight line, $P - P_0 = \langle p_s \rangle P_0(h_b + h_s)$, where $\langle p_s \rangle$ is

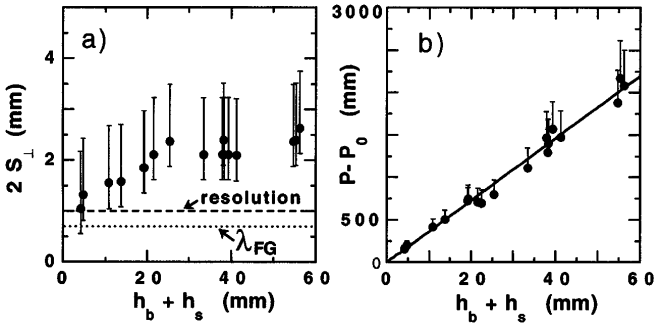

FIG. 5. The small scale structure size. (a) The average structure width $2S_\perp$ vs $h_b + h_s$. The resolution limit and λ_{FG} do not limit the measured $2S_\perp$. The error bars are due to the resolution. (b) Perimeter length vs $h_b + h_s$. Line is $P - P_0 = 0.58\ \text{mm}^{-1}\ P_0(h_b + h_s)$, where $P_0 = 62.5$ mm. Error bars of $+20\%$ P were obtained by comparing the film-density and bilevel images of the large spike in the right-hand corner of the late time image of Fig. 1 and counting the perimeter of *all* missed features. This is probably an overestimate of the true error.

the average perimeter density. The fit yields $\langle p_s \rangle \sim 0.58\ \text{mm}^{-1}$. Thus, the $2S_\perp \sim$2-mm-wide objects are distributed in such a way that, on average, each mm^2 of area in the DMZ contains $\sim$0.58 mm of perimeter at all times. Note that the edge images in Fig. 1 have the same densities of white pixels, consistent with $\langle p_s \rangle$ being constant.

The internal structure measured by $S_\perp$ and $\langle p_s \rangle$ is probably related to a cascade to small wavelengths, but the details of the cascade are difficult to measure because the smallest length scales have very little area or length. The internal structure appears after the DMZ is established, when $S_\perp$ levels off [Fig. 5(a)]. Note that numerical simulations [12,20,21,31] and Mikaelian's analytical model [11] have seen an internal structure, but it is not included in two-phase scaling models [9,15,20,28–30] although it affects the local Atwood number.

In summary, a statistically robust definition for h_b and h_s finds lower limits on $\alpha_b \approx 0.054 \pm 0.003$ and $\alpha_s \approx 0.062 \pm 0.003$ (for $A = 0.34$) consistent with recent experiments [16] ($\alpha_b = 0.061$), but still higher than in 3D simulations [10,17] or models [19] ($\alpha_b = 0.045$–0.05). The width of the large scale features scale with $h_b + h_s$, but with a wide distribution, and are narrower than models predict [15,30]. The internal structures, measured with $S_\perp$ and $\langle p_s \rangle$, appear after the DMZ has been established.

We thank J. Ticehurst, S. Kiar, D. Nelson, S. Weaver, C. Allison, and T. Schwinn for their expert technical contributions. We are grateful to Dr. E. Burke, Dr. T. Clark, Dr. F. Harlow, Dr. P. L. Miller, Dr. D. Saltz, Dr. D. H. Sharp, Dr. A. Shestakov, Dr. D. Shvarts, Dr. P. Stry, Dr. D. Youngs, and Dr. Q. Zhang for invaluable discussions. We thank Dr. M. Eckart for his support. This work was performed under the auspices of the U.S. Department of Energy by the Lawrence Livermore National Laboratory under Contract No. W-7405-ENG-48.

[1] Lord Rayleigh, *Scientific Papers* (Cambridge University Press, Cambridge, England, 1900), Vol. II, p. 200.
[2] G. Taylor, Proc. R. Soc. London A **201**, 192 (1950).
[3] E. Muller, B. Fryxell, and D. Arnett, Astron. Astrophys. **251**, 505 (1991); M. Herant and S. E. Woosley, Astrophys. J. **425**, 814 (1994).
[4] J. D. Lindl and W. C. Mead, Phys. Rev. Lett. **34**, 1273 (1975); J. D. Kilkenny *et al.*, Phys. Plasmas **1**, 1379 (1994).
[5] B. A. Remington *et al.*, Phys. Plasmas **2**, 241 (1995).
[6] D. J. Lewis, Proc. R. Soc. London A **202**, 81 (1950); J. W. Jacobs and I. Catton, J. Fluid Mech. **187**, 353 (1988).
[7] M. J. Dunning and S. Haan, Phys. Plasmas **2**, 166 (1995).
[8] D. Ofer *et al.*, Phys. Fluids B **4**, 3549 (1992).
[9] D. H. Sharp, Physica (Amsterdam) **12D**, 3 (1984).
[10] D. L. Youngs, Phys. Fluids A **3**, 1312 (1991).
[11] K. O. Mikaelian, Physica (Amsterdam) **36D**, 343 (1989).
[12] D. L. Youngs, Physica (Amsterdam) **37D**, 270 (1989).
[13] K. I. Read, Physica (Amsterdam) **12D**, 45 (1984).
[14] Y. A. Kucherenko *et al.*, in *Proceedings of the 3rd International Workshop on The Physics of Compressible Turbulent Mixing, Abbey of Royaumont, France, 1991* (CEA-DAM, France, 1992), p. 427.
[15] U. Alon *et al.*, Phys. Rev. Lett. **74**, 534 (1995).
[16] G. Dimonte and M. Schneider, Phys. Rev. E **54**, 3740 (1996).
[17] J. Hecht *et al.*, Laser Part. Beams **13**, 423 (1995).
[18] S. Atzeni and A. Guerrieri, Europhys. Lett. **22**, 603 (1993).
[19] J. Glimm and D. H. Sharp, in *Stochastic Partial Differential Equations: Six Perspectives*, edited by R. A. Carmona and B. L. Rozovskii (American Mathematical Society, Providence, 1997).
[20] J. Glimm *et al.*, Phys. Fluids A **2**, 2046 (1990).
[21] N. Freed *et al.*, Phys. Fluids A **3**, 912 (1991).
[22] G. Dimonte *et al.*, Rev. Sci. Instrum. **67**, 302 (1996).
[23] R. Aveyard *et al.*, J. Chem. Soc. Faraday Trans. 1 **82**, 125 (1986).
[24] R. Bellman and R. H. Pennington, Q. Appl. Math. **12**, 151 (1954).
[25] John C. Russ, *The Image Processing Handbook* (CRC Press, Boca Raton, FL, 1995), Chap. 5, pp. 233–249.
[26] M. B. Schneider, G. Dimonte, and B. Remington (to be published).
[27] J. Glimm, D. Saltz, and D. H. Sharp, Phys. Rev. Lett. (to be published).
[28] J. A. Zufiria, Phys. Fluids **31**, 440 (1988); U. Alon *et al.*, Phys. Rev. Lett. **72**, 2867 (1994); X. L. Li, Phys. Fluids **8**, 336 (1996).
[29] J. Glimm and D. H. Sharp, Phys. Rev. Lett. **64**, 2137 (1990).
[30] David Saltz (private communication).
[31] See images at http://esd.gsfc.nasa.gov/ESS/annual.reports/ess95contents/app.inhouse.fryxell.html